A monolithic integrated photonic microwave filter

Javier S. Fandiño[1], Pascual Muñoz[1,2], David Doménech[2] and José Capmany[1]*

Meeting the increasing demand for capacity in wireless networks requires the harnessing of higher regions in the radiofrequency spectrum, reducing cell size, as well as more compact, agile and power-efficient base stations that are capable of smoothly interfacing the radio and fibre segments. Fully functional microwave photonic chips are promising candidates in attempts to meet these goals. In recent years, many integrated microwave photonic chips have been reported in different technologies. To the best of our knowledge, none has monolithically integrated all the main active and passive optoelectronic components. Here, we report the first demonstration of a tunable microwave photonics filter that is monolithically integrated into an indium phosphide chip. The reconfigurable radiofrequency photonic filter includes all the necessary elements (for example, lasers, modulators and photodetectors), and its response can be tuned by means of control electric currents. This is an important step in demonstrating the feasibility of integrated and programmable microwave photonic processors.

Emerging information technology scenarios will require a flexible, scalable and future-proof solution for seamlessly interfacing the wireless and fibre segments of communication networks[1–3], and microwave photonics (MWP)[4,5] is the technology best positioned to achieve this target. One such scenario relates to 5G wireless communications, for which there is an ambitious range of requirements[6,7] including a 1,000-fold increase in capacity, connectivity for over 1 billion users, strict latency control, and network software programming.

These objectives call for a paradigm shift in the access network, with the incorporation of smaller cells, exploitation of the millimetre-wave regions of the radiofrequency (RF) spectrum, and implementation of massive multiple-input/multiple-output (MIMO) at base stations (BTS, base transceiver station)[7]. Integration of the wireless and fibre segments thus relies on implementing agile and reconfigurable MWP subsystems, featuring broadband operation and low space, weight and power consumption metrics. The solution is to resort to integrated microwave photonics (IMWP)[8,9] chips, allocated either in the BTS and/or the central office, combined with radio over fibre transmission in the fibre segment connecting them[10,11]. The two fundamental issues to be considered in IMWP relate to technology and architecture: (1) identifying the best material platform and (2) deciding whether to follow an application-specific photonic integrated circuit (ASPIC) approach or to use a generic programmable architecture.

So far, IMWP ASPICs have been reported mainly in four material platforms: indium phosphide (InP)[12–14], silicon-on-insulator (SOI)[15–21], silicon nitride (Si$_3$N$_4$)[22–26] and chalcogenide glass[27,28]. Several functionalities have been demonstrated with a variable degree of photonic (20–60%) integration, as shown in Table 1. A different approach is based on generic processors[29,30], where a common architecture implements different functionalities via suitable programming. A recent paper[31] reported the design of a programmable optical core inspired by the concept of electronic field programmable gate arrays. This approach is based on an optical core implemented by a two-dimensional waveguide mesh where the connections are controlled by means of tunable Mach–Zehnder interferometers (MZIs). Researchers fabricated a simplified version of the processor using a Si$_3$N$_4$ waveguide technology known as TriPleX (ref. 32). A reconfigurable processor implementing signal integration,

differentiation and Hilbert transformation has also been reported recently in InP technology[33].

To our knowledge, no contribution has yet reported the integration of all the required optoelectronic components in a single chip, either monolithically or by following a hybrid approach. Here, we report the design, fabrication and experimental demonstration of the first monolithic IMWP filter integrating all these elements into the same substrate. It includes a tunable distributed Bragg reflector laser (DBR), a dual-drive modulator, a tunable optical filter based on a ring-assisted MZI (RAMZI)[34] and a photodetector. This demonstration is a fundamental step towards the implementation of a fully programmable MWP signal processor.

Results

A MWP filter with a reconfigurable RF response can be obtained by combining a laser, an optical single-sideband (SSB) modulator, a tunable optical filter and a photodiode, as illustrated in Fig. 1a. As explained in the 'Principle of operation' section in the Methods, SSB modulation establishes a direct mapping between the optical and RF domains[35,36]. This means that the transfer function of any optical filter located after the modulator will be transferred to the RF response of the MWP filter, except for a constant amplitude and phase factor. Thus, the key to obtaining a reconfigurable photonic–RF filter is to use a tunable optical filter. This can be implemented using, for example, optical lattice architectures[34,37].

Figure 1b presents the photonic integrated circuit (PIC). Light from a tunable DBR laser (TL 1) is injected into a dual-drive Mach–Zehnder modulator (MZM). By introducing two RF signals with a 90° relative phase shift on each MZM electrode and then setting the modulator at the quadrature bias point (90°), an SSB modulation can be generated on chip. This signal is sent through an optical filter that can be reconfigured via thermo-optic heaters. The filter is based on a RAMZI architecture, where ring resonators are coupled to both branches of a symmetric Mach–Zehnder interferometer[38,39]. This filter has two inputs and two outputs. One of the inputs is used to inject the SSB signal from the modulator into the filter. The signal exists through one of the two outputs and is routed to a photodetector (PD 4). The other input of the RAMZI filter is routed with an auxiliary waveguide (called 'Input') to an optical spot-size converter located on one of the chip facets. The

Table 1 | Overview of reported IMWP chips.

Year	Reference	Functionality	Material	Components*					Photonic integration (%)
				a	b	c	e	g	
2011	12	Filter	InGaAsP/InP	R	R	R	R	R	20
				Off	Off	Off	On	Off	
2011	13	Filter	InGaAsP/InP	R	R	R	R	R	20
				Off	Off	Off	On	Off	
2013	22	Filter	TriPleX	R	R	R	R	R	20
				Off	Off	Off	On	Off	
2014	17	Filter	SOI	R	R	R	R	R	20
				Off	Off	Off	On	Off	
2015	31	Filter	TriPleX	R	R	R	R	R	20
				Off	Off	Off	On	Off	
2011	24	AWG	TriPleX	R	R	R	R	R	20
				Off	On	Off	Off	Off	
2011	18	AWG	SiN$_x$	R	R	R	R	R	20
				Off	Off	Off	On	Off	
2013	27	AWG	Chalcogenide	R	R	R	R	R	20
				Off	On	Off	Off	Off	
2013	13	AWG	InGaAsP/InP	R	R	R	R	R	20
				Off	On	Off	Off	Off	
2011	26	BFM	TriPleX	R	R	R	R	R	20
				Off	Off	Off	On	Off	
2013	15	TBPS	SOI	R	NR	R	R	R	25
				Off	NR	Off	On	Off	
2014	28	TBPS	Chalcogenide	R	NR	R	R	R	25
				Off	NR	Off	On	Off	
2013	15	TTTD	SOI	R	NR	R	R	R	25
				Off	NR	Off	On	Off	
2011	28	TTTD	TriPleX	R	NR	R	R	R	25
				Off	NR	Off	On	Off	
2013	16	TTTD	SOI	R	NR	R	R	R	25
				Off	NR	Off	On	Off	
2013	14	IFM	InGaAsP/InP	R	NR	R	R	R	25
				Off	NR	Off	On	Off	
2013	25	IFM	TriPleX	R	NR	R	R	R	25
				Off	NR	Off	On	Off	
2015	19	IFM	SOI	R	NR	R	R	R	25
				Off	NR	Off	On	Off	
2012	20	ADC	SOI	R	R	R	R	R	60
				Off	Off	On	On	On	
2016	This work	Filter	InGaAsP/InP	R	R	R	R	R	100
				On	On	On	On	On	

R, required; NR, not required; On, on chip; Off, off chip; AWG, arbitrary waveform generation; BFM, beamforming; TBPS, tunable broadband phase shift; TTTD, tunable true-time delay; IFM, instantaneous frequency measurement; ADC, photonic analog-to-digital conversion. *a, optical source; b, reconfigurable optical source shaping system; c, optical modulator; d, reconfigurable optical filtering system; e, photodetector.

same is done for the other output port, which is routed with an auxiliary waveguide (called 'Output') to another spot-size converter.

The chip was manufactured using generic InP integration technology[40] (see Methods, section 'Device fabrication and packaging'). Figure 1c–e shows a three-dimensional representation of the mask layout, a picture of a fabricated die and a picture of one of the packaged chips.

Optical lattice filters are made of a cascade of simple optical elements[34,37], such as ring resonators and MZIs. We chose an architecture based on a symmetric MZI loaded with ring resonators, known as RAMZI. A schematic diagram is shown in Fig. 2a. RAMZIs implement optimum bandpass filters (Butterworth, Chebyshev and elliptic), featuring a smaller number of optical elements than other approaches[38]. Ours was designed as a fourth-order Chebyshev type II filter, with a flat passband and ripples in the stopband. Its response is determined by the coupling between the ring resonators and the MZI branches, and by the phase shifts of the rings and the MZI arms. The custom couplers are fixed and were implemented with tapered 2×2 multimode interference couplers[41]. The optical phases can be changed by means of thermo-optic heaters.

The filter has a periodic frequency response. This periodicity is known as the free spectral range (FSR) and is determined by the perimeter of the ring resonators and the group index of the waveguides. For the InP waveguides used here, numerical simulations yielded a group index of 3.7056 at a wavelength of 1.55 μm. Thus, the ring perimeter was set to 4.0451 mm to achieve a target FSR of 20 GHz. Ideal (lossless) magnitude and phase responses, as well as simulations considering average propagation losses of 5.5 dB cm^{-1}, are presented in Fig. 2b,c, respectively.

The optical response was measured using the single-mode fibres of the package that connected the filter with the external equipment, as described in the RAMZI filter characterizations section in the Supplementary Information. Two difficulties were found during the process. First, these fibres are not polarization-maintaining, so it was not possible to prevent the excitation of both quasi-transverse electric (TE) and quasi-transverse magnetic (TM) modes. To solve this problem, a polarization alignment procedure was devised, as described in the Supplementary Information (section on the polarization alignment procedure). Second, different experiments showed that significant polarization rotation was taking place in the chip waveguides. This is also discussed in detail in the RAMZI filter characterization section of the Supplementary Information.

The MZM is a lumped modulator with two electrodes, one on each arm of the symmetric MZI. Their lengths must be less than
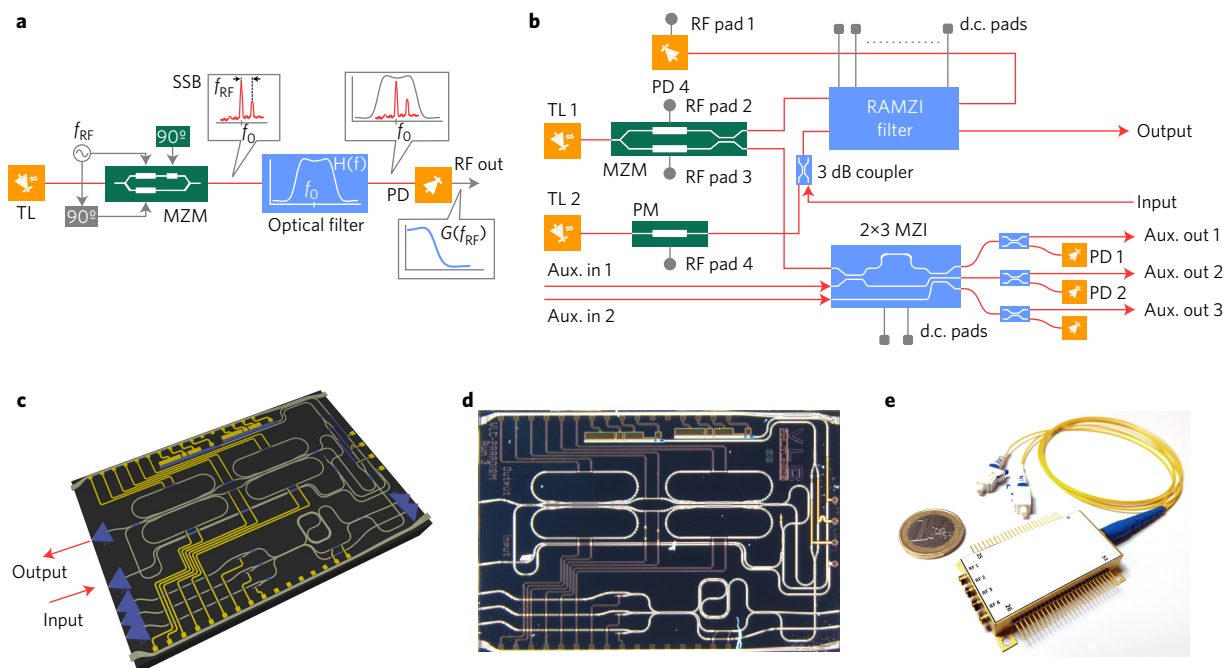
Figure 1 | Operation principle and schematic diagram of the integrated MWP (IMWP) filter. a, MWP filtering approach based on optical SSB modulation and a tunable optical filter. **b**, Schematic of the InP chip, showing all the main building blocks. **c**, Three-dimensional representation of the chip layout. **d**, Image of a fabricated die (6×4 mm^2). **e**, Packaged chip. TL, tunable laser; MZM, dual-drive Mach–Zehnder modulator; PD, photodetector; PM, phase modulator; MZI, Mach–Zehnder interferometer.

1 mm to achieve a modulation bandwidth above 10 GHz. In our case, the length was 0.68 mm. The purpose of this device is to generate SSB modulation. This requires that the RF signals driving both arms are 90° out of phase, while the modulator should be biased at the quadrature point. The exact bias voltage that needs to be applied to the modulator to be at quadrature is generally unknown. The usual procedure is to connect the two RF inputs to a broadband 90° RF hybrid and then to slowly tune the bias point while observing the modulation spectrum in an optical spectrum analyser (OSA) for a fixed modulation frequency. A bias voltage is finally chosen for which the ratio between the powers of the lower and upper sidebands is maximal. This ratio is called SSB suppression (τ) and is usually expressed in dB. The experimental set-up for the MZM adjustment is described in the Methods ('Adjustment of the dual-drive MZM' section). The experimental results are presented in Fig. 2e,f. Figure 2e shows the dependence of the median SSB suppression on bias voltage. It reaches a maximum of around 14 dB at −8 V, which is the optimum bias point. This is illustrated in the inset, where an overlap of all the measured modulation spectra (solid grey lines) is shown for this optimum voltage. They have been renormalized and shifted in wavelength, so the fluctuations of the SSB suppression around the average value can be better appreciated. The red solid line represents the average of all these responses. Finally, Fig. 2f shows the dependence of the SSB suppression on modulation frequency, keeping the optimum voltage (−8 V) and the same input RF power. The suppression is not constant with frequency. For example, it goes below 5 dB for frequencies between 9 and 11 GHz, and also shows a couple of notches around 7 and 8 GHz. This is attributed to the poor RF performance of the modulator electrodes, caused by impedance mismatch at the end of the RF line. At high frequencies, a great part of the RF power is bouncing back, creating standing wave patterns in the electrodes that are significantly affecting its broadband modulation behaviour through unwanted power and phase imbalances.

After characterizing the different components, two experiments were carried out to demonstrate the basic functionality of the

MWP filter. The first involved measuring its electro-optical (E/O) response by modulating the on-chip dual-drive MZM and afterwards detecting the signal at the output of the RAMZI filter with an external photodetector connected to one of the fibres. In this case, the effect of the PIN diode performance is therefore not included. As discussed later, a tunable low-pass MWP filter was obtained with this approach, by first adjusting the transfer function of the RAMZI filter and then tuning the central wavelength of the on-chip laser. In the second experiment, a full electrical to electrical (E/E) measurement was performed. That is, an electrical RF signal was again injected into the on-chip dual-drive MZM, and the RF output at the integrated photodetector (PD 4) was then measured. However, the presence of significant internal electrical crosstalk between the MZM and the PIN diode due to restrictions set by the packaging operation completely degraded the response of the MWP filter and thus we could not use the integrated PIN diode to measure the filter response. This is discussed in more detail in the section about the electrical to electrical (E/E) response of the MWP filter in the Supplementary Information.

A schematic diagram of the E/O experiment is presented in Fig. 3a. First, TL 1 is switched on, and a vector network analyser (VNA) and a 90° RF hybrid are used to modulate the dual-drive MZM. This is polarized at the optimum bias point (−8 V) to achieve optimum SSB suppression. The SSB modulation feeds the RAMZI filter and is afterwards collected at its output by one of the package fibres. Once the signal is outside the chip, it is split into two distinct paths by a 99%–1% optical coupler (OC). The 99% signal is injected into an OSA while the other 1% is amplified by an erbium-doped fibre amplifier (EDFA) and sent into a lightwave component analyser (LCA, Agilent N4373C).

Due to polarization rotation (described in the RAMZI filter characterization section of the Supplementary Information), the polarization of the optical signal at the input of the RAMZI filter coming from the on-chip laser is different to the one coming from an external laser source coupled to the 'Input' waveguide. Because the filter response is polarization-dependent, the RAMZI filter will
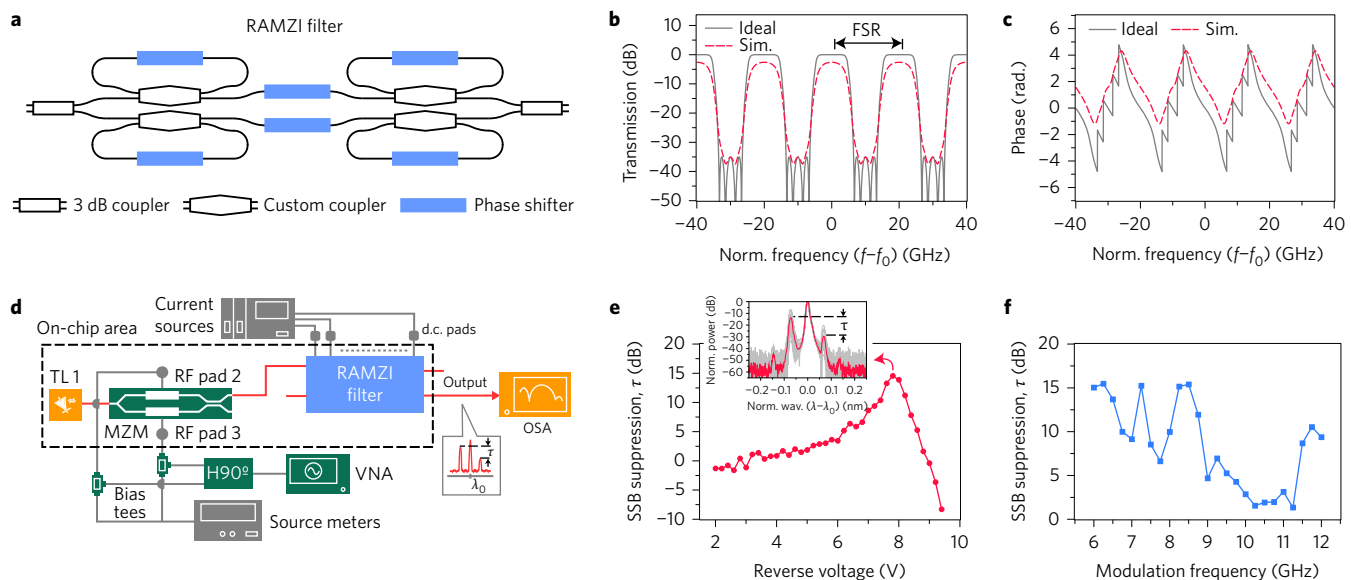
Figure 2 | RAMZI filter simulations and experimental adjustment of the dual-drive MZM. a, Diagram of the RAMZI filter. **b**, Ideal (solid grey line) magnitude response of the designed fourth-order filter and the simulated response (dashed magenta line) when considering propagation losses of 5.5 dB cm^{-1}. **c**, Similar to **f** for the phase response. **d**, Experimental set-up for determining the optimum bias point of the dual-drive MZM. **e**, Dependence of the measured median SSB suppression on applied bias voltage on one of the modulator arms, for a fixed modulation frequency of 8.5 GHz. Grey lines in the inset shows all the captured modulation spectra for the optimum bias point (−8 V), while the solid magenta line is the average of all these traces. **f**, Similar to **e**, when the bias is kept at the optimum point and the modulation frequency is swept between 6 and 12 GHz.

exhibit two different transfer functions in these two situations. This implies that the optical response of the RAMZI filter, as it is seen by the on-chip optical SSB modulation, cannot be adjusted by measuring the filter with external equipment and must be optimized instead by directly looking at its E/O transfer function. The currents injected into the thermo-optic heaters were changed until a response close to the target filter shape was obtained in the VNA. We found three distinct sets of currents (#1, #2 and #3) yielding three different, although similar, responses. Their measured E/O transmission and group delay are plotted in Fig. 3b and c, respectively. The E/O transmissions have a periodic spectral response featuring a low-pass resonance with a −3 dB bandwidth of 5.5, 5 and 3 GHz, respectively, and a FSR near 20 GHz, as shown in the inset of Fig. 3b. The band-pass resonance maximum is decreased compared to that of the low-pass resonance due to the limited bandwidth of the modulator. For band-pass filtering applications, all other passbands (including the passband at d.c.) must be eliminated, and only the passband or passbands for a particular frequency or frequencies should be kept. Note that the low-pass characteristic of this MWP filter could be suppressed with a self-beating architecture, where the optical carrier is extracted and then re-injected at the output of the optical filter before detection[42]. The filter reported here does not include this functionality. Rather, both the optical carrier and the RF sideband are jointly processed by the filter and detected afterwards. Figure 3b,c displays the calibrated transmission and group delay measurements for the baseband resonance within a range between 0 and 6 GHz, which covers the 3 dB bandwidth in all cases. The dynamic range was quantified using a standard technique (Fig. 3d,e; see Methods, 'MWP filter dynamic range' section), yielding a maximum of 81.4 dB Hz$^{2/3}$ at a modulation frequency of 1.4 GHz.

The E/O response for one of the current sets (#1) was measured for different values of the on-chip laser (TL 1) frequency. This parameter was changed by applying a small current into its phase-shifting section. The results are shown in Fig. 3f–h. Figure 3f represents the positive shift in the optical frequency of TL 1 (negative wavelength shift) as the current was increased. A shift between 0 and 4 GHz was obtained when the current

was increased from 0 to 150 μA. An overlapped representation of the laser emission spectra is shown in the inset, when no RF power was driving the modulator.

The different E/O responses obtained for each frequency in TL 1 are shown in Fig. 3g. The solid magenta line represents the initial E/O response, when no current was injected into the phase-shifting section of the laser, while the dashed, turquoise-green line is the response that corresponds with the maximum injected current (150 μA). The MWP filter exhibits a tunable low-pass behaviour, as expected, where the width of the band is reduced by increasing the laser frequency. The measured −3 dB bandwidth as a function of the tuning current is plotted in Fig. 3h. It decreases from a maximum of 5.5 GHz to a minimum of 2.5 GHz (3 GHz range). The difference between this value and the laser frequency shift, as well as the observed evolution of the RF filter shape for different currents, can be explained by both polarization rotation in the bends and the frequency-dependent SSB suppression of the dual-drive MZM. Polarization rotation is shown in the inset of Fig. 3h, where the measured polarization state of the unmodulated light coming out of the PIC during the frequency sweep is plotted on the Poincaré sphere. As the laser frequency increases, the polarization state of the signal inside the PIC changes and so the effective transfer function of the RAMZI filter as seen by the SSB modulation.

Discussion

We have reported the design, fabrication and experimental characterization of a monolithically integrated MWP filter in an InP PIC. The packaged chip includes a tunable laser, photodetectors, a dual-drive modulator, as well as a RAMZI filter tunable via thermo-optic heaters. To the best of our knowledge, this is the first monolithically integrated MWP filter reported to date. Integrated MWP filters are of special interest because of their superior tuning capabilities compared to other RF technologies. For instance, RAMZI optical filters featuring bandwidths of 1–2 GHz can be achieved using InP waveguides[12], and thus hold significant potential as the next generation of mobile wireless technologies
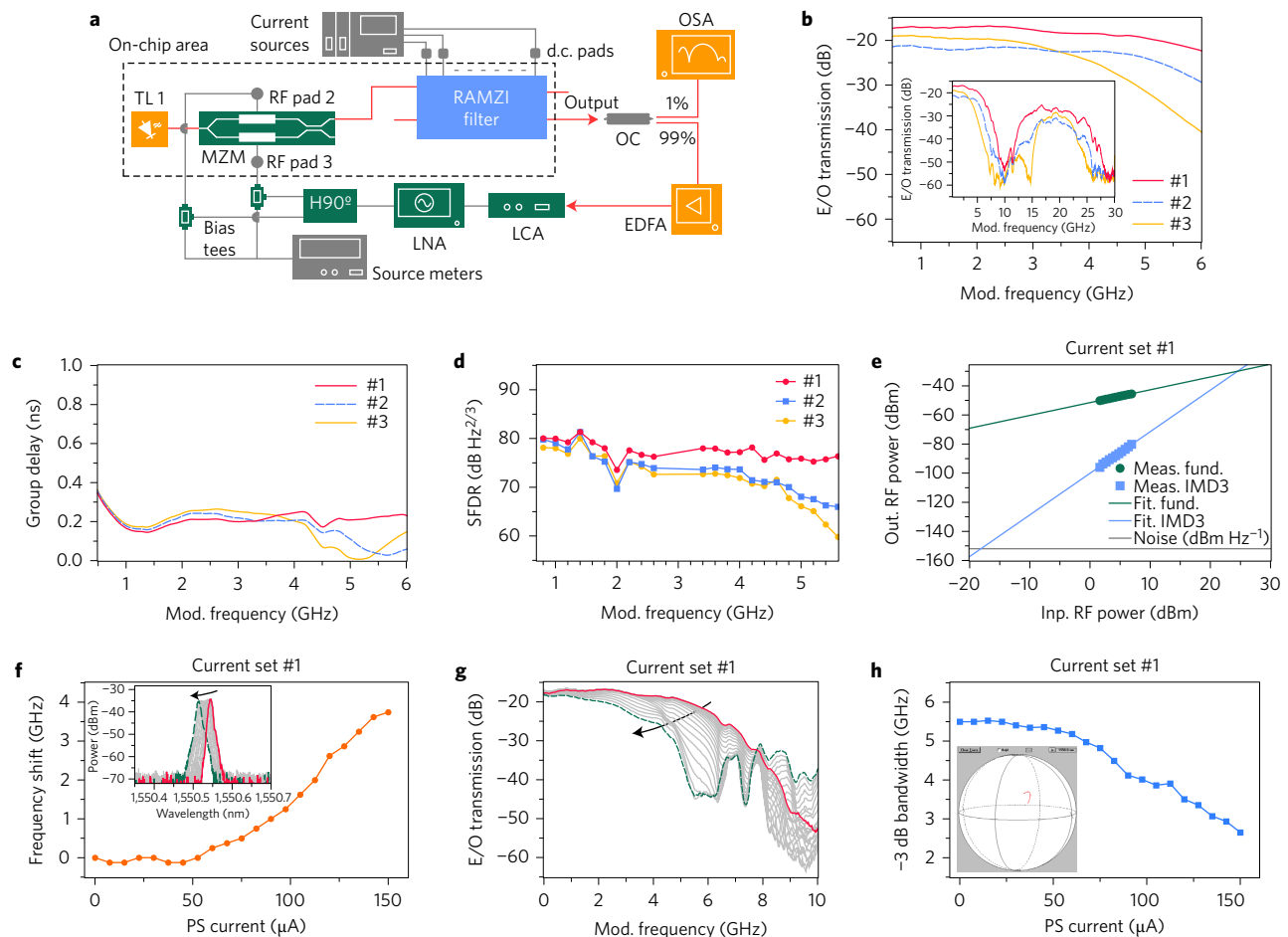
Figure 3 | Experimental results for the tunable MWP filter (E/O). a, Diagram of the experimental set-up for the E/O measurement. **b,c**, Measured E/O responses (magnitude and group delay, respectively) for three different current sets in the thermo-optic heaters (#1, #2 and #3). **d**, Measured spurious-free dynamic range (SFDR) for these three cases as a function of modulation frequency. **e**, Measured power sweep at a modulation frequency of 1.4 GHz for current set #1. **f**, Dependence of the central frequency of TL 1 with the current injected into its phase-shifting (PS) section, for current set #1. Inset: evolution of the laser emission spectrum as measured with an OSA. **g**, Evolution of the measured E/O response of the MWP filter as the frequency of TL 1 is shifted. **h**, Measured −3 dB bandwidth as a function of the current injected in the phase shifter of TL 1. Inset: measured evolution of the polarization state of the signal on a Poincaré sphere, at the output of the RAMZI filter.

(5G) is expected to move into higher frequency bands and make use of wider bandwidths. For other applications requiring sub-gigahertz bandwidth filtering, it is possible to obtain filters with narrower bandwidths by including low-gain semiconductor optical amplifiers (SOAs) inside the ring cavities. The effect of including the SOAs is to enhance the cavity quality factor by moving the filter poles closer to the unit circle[12].

During the course of the measurements, several detrimental effects, which will be fundamental in the process of implementing future integrated MWP processors, were identified and studied in more detail. In particular, a significant polarization rotation was observed in the deeply etched waveguides of the InP platform, which was later confirmed by means of simulations. This prevented external measurement of the RAMZI filter, which could not be controlled and tuned to exactly match the original design target. Severe RF crosstalk was observed when performing full electrical to electrical (E/E) measurements of the MWP filter. Nevertheless, the targeted tuning functionality was demonstrated using an electrical to optical (E/O) approach, where an auxiliary waveguide was used to inject the output of the RAMZI filter into an external photodetector. A reconfigurable low-pass filter has been demonstrated this way, with a −3 dB bandwidth tunable by 3 GHz when changing the frequency of the on-chip

tunable laser (TL 1). It must be clarified that the measured E/O results do not represent the full functionality of the chip, that is, the E/E performance, because the photodetector operation was performed by an external pin diode placed inside an LCA. Thus, only partial function of the chip has been evaluated and confirmed experimentally.

The hurdles found during the characterization stage are due to fabrication imperfections and design issues, which can be solved by a proper PIC redesign and careful dedicated manufacturing. Polarization rotation can be addressed by either reducing the sidewall angle of the waveguides or by using a much higher bending radius. RF pads should be isolated and spaced as much as possible to prevent RF crosstalk. Finally, proper termination of the dual-drive MZM arms with the right load would be beneficial to increase the performance and broadband behaviour of the SSB modulation.

Methods
Methods and any associated references are available in the online version of the paper.

References

1. Novak, D. *et al.* Radio-over-fiber technologies for emerging wireless systems. *IEEE J. Quantum Electron.* **52,** 1–11 (2016).
2. Waterhouse, R. & Novak, D. Realizing 5G: microwave photonics for 5G mobile wireless systems. *IEEE Microw. Mag.* **16,** 84–92 (2015).
3. Won, R. Microwave photonics shines. *Nat. Photon.* **5,** 736 (2011).
4. Capmany, J. & Novak, D. Microwave photonics combines two worlds. *Nat. Photon.* **1,** 319–330 (2007).
5. Yao, J. Microwave photonics. *J. Lightw. Technol.* **27,** 314–335 (2009).
6. Andrews, J. G. *et al.* What will 5G be? *IEEE J. Sel. Areas Commun.* **32,** 1065–1082 (2014).
7. Gosh, A., *et al.* Millimetre-wave enhanced local area systems: a high-data-rate approach for future wireless networks. *IEEE J. Sel. Areas Commun.* **32,** 1152–1163 (2014).
8. Marpaung, D. *et al.* Integrated microwave photonics. *Laser Photon. Rev.* **7,** 506–538 (2013).
9. Iezekiel, S., Burla, M., Klamkin, J., Marpaung, D. & Capmany, J. RF engineering meets optoelectronics: progress in integrated microwave photonics. *IEEE Microw. Mag.* **16,** 28–45 (2015).
10. Mitchell, J. E. Integrated wireless backhaul over optical access networks. *J. Lightw. Technol.* **32,** 3373–3382 (2014).
11. Liu, C., Wang, J., Cheng, L., Zhu, M. & Chang, G.-K. Key microwave-photonics technologies for next-generation cloud-based radio access networks. *J. Lightw. Technol.* **32,** 3452–3460 (2014).
12. Norberg, E. J., Guzzon, R. S., Parker, J. S., Johansson, L. A. & Coldren, L. A. Programmable photonic microwave filters monolithically integrated in InP/InGaAsP. *J. Lightw. Technol.* **29,** 1611–1619 (2011).
13. Guzzon, R., Norberg, E., Parker, J., Johansson, L. & Coldren, L. Integrated InP–InGaAsP tuneable coupled ring optical bandpass filters with zero insertion loss. *Opt. Express* **19,** 7816–7826 (2011).
14. Fandiño, J. S. & Muñoz, P. Photonics-based microwave frequency measurement using a double-sideband suppressed-carrier modulation and an InP integrated ring-assisted Mach–Zehnder interferometer filter. *Opt. Lett.* **38,** 4316–4319 (2013).
15. Burla, M. *et al.* On-chip ultra-wideband microwave photonic phase shifter and true time delay line based on a single phase-shifted waveguide Bragg grating. In *IEEE International Topical Meeting on Microwave Photonics* 92–95 (IEEE, 2013).
16. Shi, W., Veerasubramanian, V., Patel, D. & Plant, D. Tuneable nanophotonic delay lines using linearly chirped contradirectioinal couplers with uniform Bragg gratings. *Opt. Lett.* **39,** 701–703 (2014).
17. Guan, B. *et al.* CMOS compatible reconfigurable silicon photonic lattice filters using cascaded unit cells for RF-photonic processing. *IEEE J. Sel. Top. Quantum Electron.* **20,** 359–368 (2014).
18. Khan, M. H. *et al.* Ultrabroad-bandwidth arbitrary radiofrequency waveform generation with a silicon photonic chip-based spectral shaper. *Nat. Photon.* **4,** 117–122 (2010).
19. Pagani, M. *et al.* Instantaneous frequency measurement system using four-wave mixing in an ultra-compact long silicon waveguide. In *Proc. 41st European Conf. on Optical Communication (ECOC)* 1–3 (IEEE, 2015).
20. Khilo, A. *et al.* Photonic ADC: overcoming the bottleneck of electronic jitter. *Opt. Express* **20,** 4454–4469 (2012).
21. Wang, J. *et al.* Reconfigurable radio-frequency arbitrary waveforms synthesized in a silicon photonic chip. *Nat. Commun.* **6,** 5957 (2015).
22. Marpaung, D. *et al.* Si₃N₄ ring resonator-based microwave photonic notch filter with an ultrahigh peak rejection. *Opt. Express* **21,** 23286–23294 (2013).
23. Zhuang, L. *et al.* Ring resonator-based on-chip modulation transformer for high-performance phase-modulated microwave photonic links. *Opt. Express* **21,** 25999–26013 (2013).
24. Marpaung, D., Chevalier, L., Burla, M. & Roeloffzen, C. Impulse radio ultrawideband pulse shaper based on a programmable photonic chip frequency discriminator. *Opt. Express* **19,** 24838–24848 (2011).
25. Marpaung, D. On-chip photonic-assisted instantaneous microwave frequency measurement system. *IEEE Photon. Technol. Lett.* **25,** 837–840 (2013).
26. Burla, M. *et al.* On-chip CMOS compatible reconfigurable optical delay line with separate carrier tuning for microwave photonic signal processing. *Opt. Express* **19,** 21475–21484 (2011).
27. Tan, K. *et al.* Photonic-chip-based all-optical ultra-wideband pulse generation via XPM and birefringence in a chalcogenide waveguide. *Opt. Express* **21,** 2003–2011 (2013).
28. Pagani, M. *et al.* Tuneable wideband microwave photonic phase shifter using on-chip stimulated Brillouin scattering. *Opt. Express* **22,** 28810–28818 (2014).
29. Pérez, D., Gasulla, I. & Capmany, J. Software-defined reconfigurable microwave photonics processor. *Opt. Express* **23,** 14640–14654 (2015).
30. Capmany, J., Gasulla, I. & Pérez, D. Microwave photonics: the programmable processor. *Nat. Photon.* **10,** 6–8 (2016).
31. Zhuang, L., Roeloffzen, C. G. H., Hoekman, M., Boller, K.-J. & Lowery, A. J. Programmable photonic signal processor chip for radiofrequency applications. *Optica* **2,** 854–859 (2015).
32. Roeloffzen, C. G. *et al.* Silicon nitride microwave photonic circuits. *Opt. Express* **21,** 22937–22961 (2013).
33. Liu, W. *et al.* A fully reconfigurable photonic integrated signal processor. *Nat. Photon.* **10,** 190–195 (2016).
34. Madsen, C. K. & Zhao, J. H. *Optical Filter Design and Analysis: A Signal Processing Approach* (Wiley, 1999).
35. Román, J., Frankel, M. Y. & Esman, R. D. Spectral characterization of fiber gratings with high resolution. *Opt. Lett.* **23,** 939–941 (1998).
36. Hernández, R., Loayssa, A. & Benito, D. Optical vector network analysis based on single-sideband modulation. *Opt. Eng.* **43,** 2418–2421 (2004).
37. Jinguji, K. & Oguma, M. Optical half-band filters. *J. Lightw. Technol.* **18,** 252–259 (2000).
38. Madsen, C. K. Efficient architectures for exactly realizing optical filters with optimum bandpass designs. *IEEE Photon. Technol. Lett.* **10,** 1136–1138 (1998).
39. Madsen, C. K. General IIR optical filter design for WDM applications using all-pass filters. *J. Lightw. Technol.* **18,** 860–868 (2000).
40. Smit, M. K. *et al.* An introduction to InP-based generic integration technology. *Semicond. Sci. Technol.* **29,** 083001 (2014).
41. Besse, P. A., Gini, E., Bachmann, M. & Melchior, H. New 2×2 and 1×3 multimode interference couplers with free selection of power splitting ratios. *J. Lightw. Technol.* **14,** 2286–2293 (1996).
42. Pérez, D. *et al.* Figures of merit for self-beating filtered microwave photonic systems. *Opt. Express* **24,** 10087–10102 (2016).

Author contributions

J.C, J.S.F and P.M conceived the filter design. J.S.F. and D.D. designed the chip. J.S.F. conceived the experiments and performed the measurements. J.S.F., P.M. and J.C. analysed the data and wrote the paper. P.M and J.C managed the project.

Additional information

Supplementary information is available in the online version of the paper. Reprints and permissions information is available online at www.nature.com/reprints. Correspondence and requests for materials should be addressed to J.C.

Competing financial interests

The authors declare no competing financial interests.

Methods

Principle of operation. Assume that a laser with an average power P_0 and centre frequency f_0 is injected into an SSB optical modulator, which is in turn being driven by an RF tone. The tone has the following form:

$$V_{RF}(t) = A\cos(2\pi f_{RF} t) \qquad (1)$$

where A is the RF voltage amplitude and f_{RF} is the modulation frequency. The complex low-pass equivalent of the optical signal at the output of the modulator can be expressed, neglecting optical losses, as

$$\tilde{E}_{SSB}(t) = \frac{\sqrt{P_0}}{2}\left[e^{j\pi A\cos(2\pi f_{RF}t)/V_\pi} + je^{j\pi A\sin(2\pi f_{RF}t)/V_\pi}\right] \qquad (2)$$

Here, V_π stands for the π voltage of each phase shifter and we have also assumed that a 90° RF hybrid is introducing a perfect $\pi/2$ phase shift between the two RF signals that drive both arms of the SSB modulator. The modulator is also being biased at the quadrature point (90°).

Usually, A is much lower than V_π, so the small-angle approximation holds. That is, $e^{jx} = (1 - x^2/2) + jx$ for $x \ll 1$. For the sake of simplicity, second-order powers of the input signal are also neglected. Equation (2) can then be expressed as

$$\tilde{E}_{SSB}(t) = \frac{\sqrt{P_0}}{2}\left[(1+j) + j\frac{\pi}{V_\pi}Ae^{j2\pi f_{RF}t}\right] \qquad (3)$$

The Fourier transform of this waveform leads to

$$\tilde{E}_{SSB}(f) = \frac{\sqrt{P_0}}{2}\left[(1+j)\delta(f) + j\frac{\pi}{V_\pi}A\delta(f-f_{RF})\right] \qquad (4)$$

which corresponds with a single-sideband modulation. If this signal is introduced into an optical filter, then at the output we get

$$\tilde{E}_{SSB}(f) = \frac{\sqrt{P_0}}{2}\left[(1+j)H(0)\delta(f) + j\frac{\pi}{V_\pi}AH(f_{RF})\delta(f-f_{RF})\right] \qquad (5)$$

where $H(f)$ is the complex low-pass equivalent frequency response of the optical filter. That is, $H(0)$ means that the filter is evaluated at the operating wavelength of the laser (f_0, or λ_0 in the wavelength domain). The previous equation can be converted back to the time domain as

$$\tilde{E}_{out}(t) = \frac{\sqrt{P_0}}{2}\left[(1+j)H(0) + j\frac{\pi}{V_\pi}AH(f_{RF})e^{j2\pi f_{RF}t}\right] \qquad (6)$$

Finally, after detection, a time-varying photocurrent is obtained that is proportional to the modulus squared of $\tilde{E}_{out}(t)$. Neglecting the d.c. terms, and rewriting $H(0)$ as κ, the RF component is given by

$$i(t) \propto |\kappa||H(f_{RF})|\cos(2\pi f_{RF}t + \angle H(f_{RF}) + \angle\kappa) \qquad (7)$$

Equation (7) means that the RF response of the MWP filter ($G(f_{RF})$) is a scaled copy of the complex, low-pass equivalent of the optical filter transfer function ($H(f)$), multiplied by a complex constant $\kappa^\star$. That is,

$$G(f_{RF}) \propto \kappa^\star H(f_{RF}) \qquad (8)$$

As a consequence, a direct mapping between the optical and RF domains is obtained.

Device fabrication and packaging. The designed PIC was manufactured within the European FP7 project PARADIGM (FP7-ICT-2009-5/257210). The PARADIGM initiative aimed to facilitate access to state-of-the-art InP foundries following a generic approach, that is, by providing external users with a set of predefined components that are not trivial to design and then sharing the cost of PIC fabrication via multi-project wafer runs. In this case, the chip was manufactured in a non-insulating InP platform offered by the company Oclaro. Deeply etched waveguides are made of an n-doped InP substrate over which an InGaAsP multi-quantum well structure is grown, forming the waveguide core. Afterwards, the core region is covered with a layer of p-doped InP. Finally, the whole structure is etched by ~3.6 μm from the top of the p-doped region. The deep etch results in high mode confinement, which allows for a tight bending radius of 150 μm. In this case, a waveguide width of 1.5 μm was used. According to the available data, it should experience propagation losses of ~5.5 dB cm^{-1}. Angled spot-size converters with both vertical and lateral tapers were also provided, featuring estimated coupling losses below 1 dB. Note that the diagram in Fig. 1b includes more components that those strictly required for implementing the MWP filter, such as an extra tunable DBR laser (TL 2), a phase modulator (PM) and a tunable 2×3 MZI with three d.c. photodiodes located at its output (PD 1, PD 2 and PD 3). These were used as auxiliary elements during characterization of some important devices for filter

operation, such as the thermo-optic heaters. Experimental results are provided in the Supplementary Information (section on building block characterization).

The PIC was packaged to facilitate its characterization. This service was offered by some partners of the PARADIGM consortium, and in this case was done by the Linkra. The PIC layout was designed to meet the requirements imposed by the standard packaging process. The layout was created using process design kit libraries with commercial software by PhoeniX. This sets a maximum number of optical inputs/outputs, d.c. and RF pads, and specifies a predefined location for all of them (Fig. 1c–e). A maximum of 48 d.c. pads can be used, all of which are located on the upper/lower facets of the die. Up to four RF pads are also available to the designer, all located close to the right chip facet. Up to two standard single-mode fibres can be coupled to on-chip spot-size converters, which are located on the left chip facet. Inside the metallic enclosure, the RF pads are wire-bonded to a ceramic substrate that routes the RF signals to external Gilbert push-on connectors (d.c. to 65 GHz). The d.c. pads are also wire-bonded and then connected to a set of equally spaced pins in the external metallic case. A thermistor and a Peltier cell are included in the package to provide accurate temperature control.

Adjustment of the dual-drive MZM. The layout of this PIC poses an extra difficulty for the optimization of the MZM, because the optical spectrum measured at the output fibre is not that of the modulator itself, but that of the modulated signal after passing through the RAMZI filter. As a consequence, the measured SSB suppression ratio does not match the real ratio at the output of the modulator, which is required to obtain the bias point. An alternative approach to solve this issue was devised, which is described in the following.

The experimental set-up used to find the optimum bias point of the MZM is shown in Fig. 2d. A microwave VNA (Agilent PNA-X, N5245A, 10 MHz–50 GHz) first generates an RF tone with constant amplitude and frequency. This tone is injected into a 90° RF hybrid (Marki microwave, QH0R714, 0.7–14.5 GHz), the two outputs of which are then connected to a couple of broadband bias tees (SHF Communications, SHF-BT-45-D, 20 kHz–45 GHz). In turn, they are used to drive the two ports of the dual-drive MZM (RF pads 2 and 3 in Fig. 1b). For each reverse bias voltage in one of the MZM arms, we apply a different set of independent, uniformly distributed random currents in the thermo-optic heaters of the RAMZI filter, and finally capture the modulation spectrum exiting through the output fibre. The power ratio between the lower and upper sidebands (τ) is measured and stored for each current set. It is expected that the measured ratio will fluctuate up and down due to the influence of the RAMZI filter, which is changing for each set of random currents. However, if a sufficiently high number of modulation spectra are measured, then the median ratio extracted from these measurements will converge to the real value (that is, the real SSB suppression as would be measured at the output of the modulator). In the experiment, a tone of +5 dBm and a frequency of 8.5 GHz was used to modulate the MZM. A constant reverse voltage of −2 V was applied in one of the MZM arms, while the bias in the other arm was swept between 2 and 9.4 V in steps of 0.2 V. For each bias value, we applied a set of 25 different, independent, uniformly distributed random currents in the six thermo-optic heaters of the RAMZI filter and the output spectrum was captured in an OSA (Advantest Q8384).

MWP filter group delay. Group delay in MWP filters is usually measured using a phase-shift approach[43] where an external tunable continuous-wave (c.w.) laser is modulated by a Mach–Zehnder intensity modulator driven by an RF signal with relatively low frequency (10–50 MHz) supplied by a VNA. The optical signal is then fed to the filter, downconverted to RF in a photodetector, and fed to the VNA, which measures the RF-to-RF response. By sweeping the wavelength of the c.w. laser one obtains a complete spectral characterization. In our case, because the tunable laser was integrated in the chip we had to sweep the RF signal frequency. This approach leads to poor resolution for double sideband modulation (DSB) signals but is valid for SSB modulation, as in our case. The measured group delay response is obtained after correcting for the calibration of the external optical and RF components employed in the experimental set-up of Fig. 3a.

MWP filter dynamic range. To quantify the linearity of the MWP filter, the VNA in the experimental set-up of Fig. 3a was temporarily replaced by a vector signal generator (Agilent, E8267C), while the signal at the output of the LCA was connected to a RF spectrum analyser (Agilent, N9020A). A standard two-tone test was then performed, increasing the RF power of two closely spaced tones (500 kHz) at the input of the modulator, while measuring the power at the output of the LCA. Figure 3d shows the measured third-order spurious-free dynamic range (SFDR) for the three filter configurations (#1, #2 and #3) as a function of modulation frequency. The power sweep for current set #1 at a modulation frequency of 1.4 GHz (best case) is plotted in Fig. 3e, as an example. The noise floor was around −150 dBm Hz^{-1}, limited by the electrical noise of the LCA and the RF spectrum analyser.

References

43. Zhuang, L. *et al.* Novel low-loss waveguide delay lines using Vernier ring resonators for on-chip multi-λ microwave photonic signal processors. *Laser Photon. Rev.* **7,** 994–1002 (2013).